Mon. Not. R. Astron. Soc. **463**, 3339–3353 (2016) Printed 19 December 2016 (MN LATEX style file v2.2)

Radio-Optical Galaxy Shape Correlations in the COSMOS Field

Ben Tunbridge⋆, Ian Harrison, Michael L. Brown
Jodrell Bank Centre for Astrophysics, School of Physics and Astronomy, The University of Manchester, Manchester M13 9PL, UK

arXiv:1607.02875v2 [astro-ph.GA] 16 Dec 2016

19 December 2016

ABSTRACT

We investigate the correlations in galaxy shapes between optical and radio wavelengths using archival observations of the COSMOS field. Cross-correlation studies between different wavebands will become increasingly important for precision cosmology as future large surveys may be dominated by systematic rather than statistical errors. In the case of weak lensing, galaxy shapes must be measured to extraordinary accuracy (shear systematics of $< 0.01\%$) in order to achieve good constraints on dark energy parameters. By using shape information from overlapping surveys in optical and radio bands, robustness to systematics may be significantly improved without loss of constraining power. Here we use HST-ACS optical data, VLA radio data, and extensive simulations to investigate both our ability to make precision measurements of source shapes from realistic radio data, and to constrain the intrinsic astrophysical scatter between the shapes of galaxies as measured in the optical and radio wavebands. By producing a new image from the VLA-COSMOS L-band radio visibility data that is well suited to galaxy shape measurements, we are able to extract precise measurements of galaxy position angles. Comparing to corresponding measurements from the HST optical image, we set a lower limit on the intrinsic astrophysical scatter in position angles, between the optical and radio bands, of $\sigma_\alpha > 0.212\pi$ radians (or 38.2°) at a 95% confidence level.

Key words: radio continuum: galaxies – cosmology: observations – gravitational lensing: weak

1 INTRODUCTION

Weak gravitational lensing analyses exploit the coherent distortion of galaxy shapes induced by the gravitational potential along the line of sight to constrain the distribution and evolution of massive structures in the Universe, providing an excellent probe of cosmology (see e.g. Kilbinger 2015, for a review). Conducting precision cosmology tests with weak lensing (e.g. selecting between competing models of dark energy) requires high number densities ($n_{\rm gal} \gtrsim 1\,{\rm arcmin}^{-2}$) of high redshift ($z \gtrsim 1$) sources and analysis tools to measure their shapes to extraordinary accuracy. These attributes have been available to surveys at optical wavelengths for a number of years, with useful cosmological results beginning to emerge from CFHTLens (Köhlinger et al. 2016), DES-SV (The Dark Energy Survey Collaboration et al. 2015) and DLS (Jee et al. 2015). As source number densities increase in these and future experiments (and statistical uncertainties decrease) it is the systematic uncertainties which will come to dominate. One way of tackling the problem of such systematics is through multi-wavelength investigations, which have the potential to address both instrumental and astrophysical contamination. In particular, telescopes operating at radio wavelengths are about to undergo a significant leap in survey speed and sensitivity and, ultimately, with the Square Kilometre Array (SKA)[1] will be capable of world-leading weak lensing cosmology alone (Brown et al. 2015; Bonaldi et al. 2016). In addition, cross-correlation weak lensing studies between radio and optical wavebands appear highly promising, providing comparable cosmological constraints as traditional single-waveband experiments, but with the significant advantage of being much more robust to wavelength-dependent systematic effects (Demetroullas & Brown 2016; Harrison et al. 2016).

In this paper we focus on a particular aspect of these cross-correlation studies: the correlation between the optical and radio shapes of those galaxies which will be common to both catalogues. As discussed in Harrison et al. (2016) this

⋆ E-mail: benjamin.tunbridge@manchester.ac.uk

[1] http://www.skatelescope.org

© 2016 RAS

shape co-variance constitutes a noise term on the measured weak lensing shear power spectra, and needs to be well understood to form robust cosmological parameter constraints. Furthermore, literature results on these shape correlations are divided, with Battye & Browne (2009) finding a significant correlation in orientations between the shapes of objects detected in the SDSS and FIRST catalogues, and Patel et al. (2010) finding almost no correlation in the optical and radio shapes of galaxies in the Hubble Deep Field North (HDF-N). Here we measure and compare the optical and radio shapes of sources in the COSMOS field, which has deep data available in both wavebands. To facilitate an accurate comparison, we have implemented a significant re-analysis of the radio VLA-COSMOS data set. Our re-analysis significantly reduces the level of galaxy shape systematics which we found to be present in the previous analysis of Schinnerer et al. (2007) (though we note that their analysis was primarily focused on measuring faint number counts and was not optimised for extracting galaxy shapes).

When conducting any study which relies upon accurate galaxy shape measurements, it is important to appreciate that the data generated in radio observations is fundamentally different to that generated by imaging telescopes in optical wavebands. Radio telescopes are typically operated as interferometers, consisting of many individual antennas, from which the signals are correlated to form 'visibilities'. For a pair of antennas a projected distance d apart, the recorded visibility is a measurement of the flux at a specific spatial frequency on the sky. For interferometers with N antennas, $N(N-1)/2$ correlations can be formed between the different baseline lengths, sampling a large number of scales and allowing us to reconstruct a partially sampled Fourier transform of the sky brightness distribution (when the assumptions of the Van Cittert-Zernike theorem, Carozzi & Woan 2009, are satisfied). This can provide distinct advantages, allowing for very good angular resolution (set by the longest baseline in the array) with a comparably large maximum field of view (set by the primary beam of the individual antennas).

The incomplete sampling of spatial scales means the data must be further processed to obtain an estimate of the corresponding image plane information. The resultant Point Spread Function (PSF) from a radio interferometer (commonly referred to as a 'dirty beam') is highly deterministic at $\gtrsim 700\,\mathrm{MHz}$ frequencies (as it is set by the known sampling of the Fourier plane – a useful property for weak lensing) but can have significant structure, with appreciable sidelobes extending across the entire sky. The convolution of this complicated beam with an unknown sky creates the 'dirty image' (the simple Fourier transform to image space of the data). Deconvolving the dirty beam from the dirty image to enable source identification, flux and shape measurement is then a difficult process.

A commonly used algorithm for this purpose is known as Högbom-CLEAN. This algorithm assumes that any section of the sky is made up of a finite number of delta function point sources. Beginning with the dirty image, CLEAN iteratively finds the position and brightness of the brightest source in the field and subtracts flux, corresponding to the convolution of this point source with the dirty beam, directly from the visibility data. This is repeated across the image until a residual map remains with CLEAN components, and produces a 'CLEAN' map (see Högbom 1974, for a detailed description and motivation). Additionally this procedure helps to reduce sidelobe artifacts across the radio map which can be problematic, especially when a large dynamical range in source fluxes is considered.

The CLEAN algorithm works well at producing plausible radio images and placing sources at reliable positions. However CLEAN is a non-linear deconvolution technique which assumes that missing information, due to a partially sampled visibility (or Fourier) plane, can be modelled as a set of point sources. This inherent assumption may result in significant systematics when attempting to measure precision morphology as is necessary for weak lensing cosmology. Patel et al. (2015) have tested the performance of CLEAN on SKA-like simulations and have found the performance to be orders of magnitude away from what is necessary for systematic uncertainties from shape measurement to be sub-dominant to statistical ones when measuring cosmic shear. In this paper, we have adopted a CLEAN-based imaging pipeline in our re-analysis of the VLA-COSMOS data. However, mindful of the above concerns around potential shape biases being induced by the CLEAN processing, we have also carried out extensive simulations to quantify the level of shape measurement bias we expect in our newly-created image.

In addition to minimising systematics through cross-correlation, radio weak lensing also presents further potential advantages through additional information from polarisation (Brown & Battye 2011; Whittaker et al. 2015b) and rotational velocity maps (Morales 2006) which may be used to reduce the shot noise from intrinsic galaxy shapes and also mitigate against intrinsic alignment systematics – a key astrophysical systematic due to correlations of galaxy shapes being imprinted during their formation process. To date two attempts have been made to measure a weak lensing signal in radio data alone. In the first, Chang et al. (2004) were able to detect a lensing aperture mass signal at a significance of 3.6σ. In this case the Fourier-plane data from the FIRST radio survey (Becker et al. 1995) was used to estimate the shear on radio sources directly, without imaging, modelling them using Fourier-plane shapelets (Chang & Refregier 2002). The second study, by Patel et al. (2010), used combined radio observations from the VLA and MERLIN interferometers to extract galaxy shapes from radio images constructed by the Högbom-CLEAN method discussed above, where the low absolute number of detected sources precluded a significant weak lensing detection.

This paper is structured as follows. In Section 2 we introduce the COSMOS data used in this study and outline the data reduction steps that we have applied. In Section 3, we describe our technique for creating simulated radio datasets and we also describe our approach to measuring the radio galaxy shapes, which includes the extraction of a model of the VLA-COSMOS PSF from the simulated datasets. An assessment of the accuracy of the shape parameter recovery from the radio simulations is provided in Section 4. In Section 5 we present the shape measurements from the real VLA-COSMOS data. We then investigate the correlation between the radio-derived and optical-derived position angles of galaxies within the COSMOS field in Section 6. Finally, in Section 7 we summarise our conclusions.

2 DATA

The COSMOS field is a $2\,\mathrm{deg}^2$ patch of sky which has already been subject to extensive multi-wavelength analysis, with data available from a large number of telescopes including the Hubble Space Telescope (HST, optical), the Very Large Array (VLA, radio), as well as the Spitzer (infrared), GALEX (UV), and XMM/Newton (X-ray) satellites. In this study we focus on the radio and optical observations, taken with the VLA at L-band (1.4 GHz) in A- and C-array configuration, and with the Advanced Camera for Surveys (ACS) instrument onboard the HST, respectively.

2.1 VLA radio observations

The VLA L-band observations consist of a combination of A- and C-array observations sub-divided into two intermediate frequency (IF) chunks which are centred at 1.3649 and 1.4351 GHz, with each of the IFs further divided into 6 channels each averaging over a 3.125 MHz bandwidth. The combination of the A- and C-array observations allows a wider range of spatial scales to be probed. (The accessible spatial scales are dependent upon antenna configuration – A-array corresponds to smaller scales, and C-array to larger scales in this case). The observation time totals 240 hours and 19.5 hours in A- and C-array configurations respectively. In total 23 pointings were required to cover the COSMOS field, providing a separation of $15'$ between the individual field centres. The VLA observations and accompanying data reduction and imaging was initially conducted by Schinnerer et al. (2007), where more information on the observation strategy can be found.

We performed an initial examination of the radio image as produced by Schinnerer et al. (2007) in order to assess its suitability for extracting galaxy shapes.[2]. The results of this assessment are illustrated in Figure 1, which shows a histogram of the position angles (α) of all resolved sources detected in the image. To extract the galaxy shapes, we used the IM3SHAPE package (Zuntz et al. 2013), described in further detail in Section 3. Note that in this study we define α to be the position angle of the galaxy measured North of East (i.e. counter-clockwise).

In the absence of lensing and/or intrinsic alignment effects, we expect the galaxies to be randomly orientated and the position angle histogram to be consistent with a uniform distribution. Clearly, a large deviation from the expected random uniform distribution is observed. This is likely to be due to systematic effects introduced during the image creation and/or shape measurement steps. For example, as discussed in Section 1, we expect systematic effects to be introduced at some level due to the use of the CLEAN-based imaging routine – the AIPS task 'IMAGR'[3] – that was used in the creation of the Schinnerer et al. (2007) image. Noting again that the Schinnerer et al. (2007) study was not focused on shape measurements, and motivated by the results shown in Figure 1, we have performed our own imaging analysis of the VLA-COSMOS visibility data. While our reanalysis also makes use of the CLEAN algorithm, implementing the data reduction and imaging ourselves enables us to accurately quantify the shape measurement bias due to the imaging pipeline through simulations.

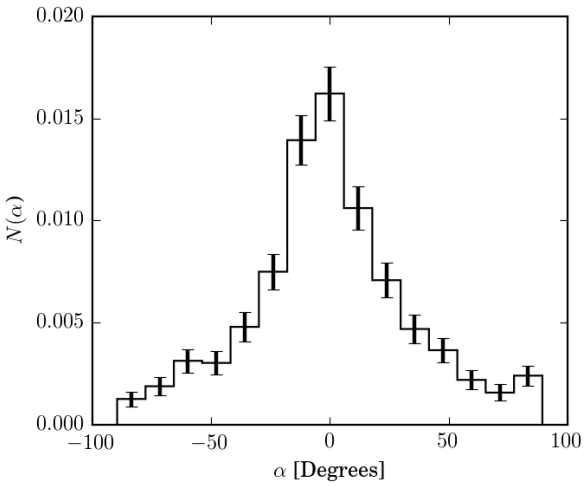

Figure 1. A histogram of the position angles of all resolved sources detected in the VLA-COSMOS radio image of Schinnerer et al. (2007). The galaxy position angles (α) were measured using the IM3SHAPE shape measurement software. The measured distribution is clearly inconsistent with the expected random uniform distribution. Poisson error bars are included.

2.1.1 *Data Reduction*

For the purposes of this work, we require a precise quantification of any shape systematics caused by the data reduction and imaging processes. This necessitates the use of the simulations detailed in Section 4 and the construction of a coherent pipeline which may be run identically on both simulations and real data. For the radio data we begin from partially processed continuous visibility data provided to us by E. Schinnerer and V. Smolcic (via private communication with C. Hales). Although this data was partially reduced, we found it necessary to apply further data reduction steps in order to arrive at a fully reduced and calibrated visibility dataset.

We have used the Common Astronomy Software Applications (CASA; McMullin et al. (2007)) packages, following the calibration steps outlined in Taylor et al. (1999), and implemented in Schinnerer et al. (2007).

We first removed Radio Frequency Interference (RFI) from the data by flagging visibilities which contained RFI at higher levels than the sky signal. After clipping the data to remove all entries with amplitude $> 0.9\,\mathrm{Jy}$ we further visually inspected the data to remove structures corresponding to RFI. The amount of data removed was 9.9% of the initial data. The remaining (u, v, w) locations are then used throughout the rest of our analysis, including for the simulations.

Calibration errors in the visibilities were accounted for by intercalated observations of calibration sources with known fluxes and morphologies, with the calibration solutions interpolated on to the observations of the target field.

[2] We performed this assessment on the publicly available image produced by Schinnerer et al. (2007), which we downloaded from `http://www.mpia.de/COSMOS/`.
[3] Wide field imaging algorithm via the Högbom-CLEAN method.

Three calibration sources were observed: primary flux calibration source 0521+166; primary phase calibrator 1024-008; and, as a secondary calibrator in both flux and phase, 0925+003.

We proceeded through a series of reduction steps from a standard radio astronomy data reduction cookbook as described in, for example Fomalont & Perley (1999):

- Delay (phase) calibration
- Initial bandpass calibration
- Gain calibration of calibration sources
- Flux derivation for calibration sources
- Bandpass calibration with spectral indices
- Update amplitude and phase calibration solutions
- Apply calibration solutions to target fields

The result of these steps was initially calibrated visibility data, ready for image-plane calibration and final imaging, as described in the next section.

2.1.2 Imaging

Provided with the calibrated visibilities for all 23 VLA pointings we developed an imaging pipeline implemented as a series of CASA tasks. Each of the 23 pointings was imaged separately using the CLEAN task, which deconvolves the complex radio interferometer beam following the Högbom-CLEAN algorithm introduced in Section 1, and described further in Högbom (1974).

Residual sidelobe noise from one bright source (RA 10:02:51.242, DEC +2:42:48.70) was removed from multiple pointings using a technique known as 'peeling'. Peeling is a form of direction-dependent calibration which involves using the best available model to subtract all other sources from the data except the off-axis peeling target. The technique then models only the off-axis source (via self-calibration) before subtracting the fitted model from the original data set with all sources included. A detailed description can be found in Noordam (2004). When imaging the data, we ran the pipeline using two separate weighting schemes in order to evaluate the effectiveness of both. These weighting schemes are used in gridding – the step which places the continuous visibilities onto a regular grid amenable to Fast Fourier Transforms – and the choice of a particular scheme can affect the radio map on the arcsec scales to which we are sensitive. 'Natural' weighting equally weights all of the continuous visibilities and optimises for point-source sensitivity (but sacrifices resolution), whilst 'uniform' weighting inversely weights according to the density at which the UV plane is being sampled, and optimises for resolution at the expense of sensitivity (Taylor et al. 1999).

Since each pointing has a relatively large field of view (radius of $20.8'$), curvature across the field of view needs to be accounted for: the Fourier transform performed by the interferometer is no longer in two dimensions (u, v) only but includes a third w term. To account for this, we use the 'WPROJPLANES' tool within CLEAN to automatically assign w-projection planes for convolution of non-coplanar effects (see Cornwell et al. 2008, for a full description of w-projection).

For each weighting scheme (natural and uniform), the data was gridded onto pixels corresponding to $0.35''$ in the image plane and covering the full primary beam field of view.

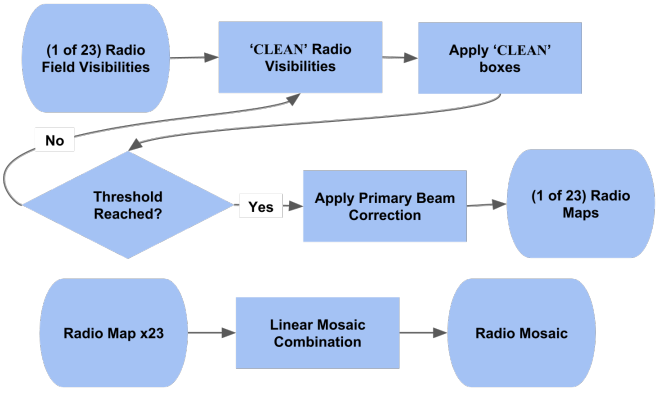

Figure 2. A flow chart depicting the radio imaging pipeline. Each of the 23 fields are first run through the top rung. Following this the 23 fields are combined into a linear mosaic.

'CLEAN BOXES' were interactively added to areas of likely identified bright sources to assist the imaging algorithm, and this was repeated as more sources became visible in the residual map. A loop gain of 0.05 is applied during each iteration. This iterative imaging process was regarded as converged either after $100,000$ iterations, or when the RMS of the residual image after model subtraction was $< 45\,\mu$Jy.

For each pointing, the output of the above procedure was a map of the entire field of view ($16,000 \times 16,000$ pixels). To this map, we applied a correction for the primary beam pattern using a gain level of 0.5, which corresponds to a radius of $20.8'$. Finally the 23 individual pointings were combined into a mosaiced image using the IMAGER.LINEARMOSAIC tool. Our imaging pipeline is shown schematically in Figure 2 and a full list of CLEAN inputs can be found in the imaging pipeline script available at `https://github.com/bentunbridge/cosmos-radio-optical`.

The image produced using natural weighting has a beam central lobe size with a full width at half maximum (FWHM) of $1.5'' \times 1.4''$, at an orientation of $70°$, while the image obtained using uniform weighting has a beam central lobe size with FWHM $1.45'' \times 1.3''$ at an orientation of $-20°$. The position angles here are defined in a counter-clockwise sense, North of East. One could, in principle, use these recovered beam parametrisations as an approximation to the observational PSF during galaxy shape estimation. However as shown in Section 3.1 this can be improved upon by directly measuring the PSF from images reconstructed from simulations that include injected unresolved sources (point sources) placed across the field. The RMS noise level in our final mosaiced image was 33 (59) μJy/beam and 28 (52) μJy/beam in the central 1 (2) deg^2 region of the field for the natural (uniform) weighting scheme. Although this is ~ 3 times the noise level achieved in the Schinnerer et al. (2007) study we find only a minor drop in resolved source counts ($\sim 6\%$) while, as we demonstrate in Section 4, we find our image is more robust in terms of shape systematics effects. Implementing our own data reduction and imaging pipeline also allows us to accurately model any analysis-induced systematic effects through simulations.

2.2 HST-ACS survey data

For our optical shape measurements, we use the observations collected with the ACS instrument on board the HST, as described in Koekemoer et al. (2007). These observations were conducted over a total of 583 HST orbits, covering a field that is 1.64 deg^2 in area.

The observations were collected using the F814W filter and reach a limiting magnitude of $I_{AB} = 27.2$ mag at 10σ, and the angular resolution is 0.05 arcsec (McCracken et al. 2010). The science data used in this study was produced by Koekemoer et al. (2007) and consists of 575 pointings across the entire mosaic. Additionally, for each pointing the raw exposures were combined using the MultiDrizzle pipeline (Koekemoer et al. 2003) to improve the pixel scale to 0.03 arcsec, which we use in our analysis. The output MultiDrizzled image cutouts are available at `http://irsa.ipac.caltech.edu/Missions/cosmos.html`.

3 SHAPE MEASUREMENTS

3.1 Modelling the effective radio PSF using simulations

To date, many shape measurement techniques have been developed and optimised for weak lensing surveys, predominantly at optical wavelengths. A key systematic effect to account for in these techniques is the correct deconvolution of the PSF of the observations, and it is equally important to account for such effects in radio observations. As discussed in Section 1, the PSF applied to the sky (the 'dirty beam') by a radio interferometer is precisely known and highly deterministic (and mostly unaffected by stochastic variation in the atmosphere). However, this is only the correct PSF for the dirty map and has significant sidelobes across the entire sky, meaning almost all sources are blended with one another. Deconvolving this PSF correctly is a challenging task. The CLEAN algorithm is one approach to performing the deconvolution. However, as discussed in Section 1, CLEAN is highly interactive and non-linear, meaning that by the time a CLEAN image has been produced, the effective PSF in the image is some unknown function, usually modelled as a Gaussian fit to the central lobe of the dirty beam (and known as the 'CLEAN beam').

For source morphology this leads to un-modelled shape distortions due to the PSF which are not captured by the CLEAN beam. To account for this additional distortion, we use simulations of the VLA COSMOS dataset to estimate an effective PSF model in the image plane. We additionally use these simulations to probe for shape systematic effects induced by the imaging pipeline.

The input sky image used for the simulation was created with the GalSim (modular galaxy image simulation) toolkit (Rowe et al. 2015). Our simulations include the positions and morphologies of all sources identified in the source catalogue constructed by Schinnerer et al. (2007). We note that it is primarily the distribution of source positions, fluxes and sizes which determines the characteristics of the un-CLEANed flux contributing to the residual distortions in the effective PSF in the image. By using the Schinnerer et al. (2007) catalogue as input to our simulations, we ensure that the position, flux and size distributions of sources in our simulations are approximately the same as the true distributions in the COSMOS field. The catalogue of Schinnerer et al. (2007) was constructed using the AIPS tasks 'SAD'[4], 'MAXFIT'[5] and 'JMFIT'[6] to determine the source position, flux density and morphologies.

We generate the resolved sources in our simulations assuming elliptical Gaussian morphologies, and using the best-fit parameters as determined by Schinnerer et al. (2007). For all sources that were classified as unresolved by Schinnerer et al. (2007), we inject a single pixel source (delta function) with the appropriate flux and position into the simulation. The simulations are created on a real-space grid with a pixel scale of $0.2''$/pixel, which is higher resolution than that of the final radio image which is gridded to $0.35''$/pixel. For each of the 23 COSMOS field pointings we project this simulation onto the visibilities corresponding to the true Fourier plane sampling of the original VLA dataset. Finally, random noise (with RMS equal to that measured from the real visibility data) is added to the simulated visibilities.

The simulated visibility data sets thus contain the same dirty beam, the same level of random noise, and approximately the same source distribution as was found in the original data set. Additionally, the resolved source morphologies are exactly known and can serve as a test of the imaging pipeline. The simulated datasets were then processed using the exact same imaging pipeline as described in Section 2.1.2, using the CASA task CLEAN. The output of our simulation pipeline is thus a re-constructed CLEAN image which should fully capture any systematic effects introduced by the radio imaging process.

By examining the observed shapes of those objects that were injected as point sources, we were then able to estimate the effective PSF across the image. In order to capture any spatial variation in the PSF, the field was split into a 4×4 grid and a weighted mean of the measured shapes corresponding to the injected point sources was calculated in each of the 4×4 grid cells. We used the signal to noise ratio (S/N) as the weight for each source,

$$\mathrm{PSF}_{\mathrm{Total}} = \frac{1}{\sum_i \omega_i} \sum_i \omega_i I_i, \quad (1)$$

where $\omega_i = (S/N)_i$. We found that the resulting weighted mean beam shapes in each grid cell were well modelled using 2D Gaussian ellipses though the PSF shape did vary somewhat across the field. Note that we extracted estimates of the PSF from the simulations for the natural and uniform weighting schemes separately. Cut-outs of the final PSF model images were produced with a 32×32 stamp size (equivalent to a 11.2×11.2 arcseonds), and were later up-sampled[7] to 170×170 cut-outs. These PSF cut-outs were subsequently used in the shape analysis of both the resolved simulated sources, and of the resolved real sources.

[4] 'SAD' (Search and Destroy) is a source extraction program within AIPS.
[5] 'MAXFIT' is a coordinates and value extremum finder algorithm within AIPS, useful for finding the centre position of sources.
[6] 'JMFIT' is a Gaussian fitting algorithm within AIPS.
[7] The original cut-outs were upsampled from the original sidelength of $s = 32$ pixels to an upsampled sidelength $S = 170$ pixels, using a padding co-efficient of $p = 2$ and an up-sampling coefficient of $u = 3$, following the relation $S = (s + p) \times u$.

	Natural Weighting				Uniform Weighting			
Grid Number	a [arcsec]	b [arcsec]	α [deg]	$\boldsymbol{e}$	a [arcsec]	b [arcsec]	α [deg]	$\boldsymbol{e}$
1	1.404	1.385	22.1	0.0135	1.320	1.235	19.4	0.0664
2	1.449	1.449	45.0	0.0001	1.386	1.314	25.6	0.0536
3	1.386	1.385	41.8	0.0009	1.357	1.301	16.5	0.0419
4	1.411	1.409	39.5	0.0012	1.330	1.287	23.5	0.0335
5	1.380	1.371	37.4	0.0066	1.336	1.234	20.8	0.0780
6	1.381	1.339	33.2	0.0311	1.327	1.250	18.5	0.0589
7	1.388	1.383	37.6	0.0037	1.327	1.253	17.6	0.0574
8	1.396	1.361	33.2	0.0257	1.315	1.250	18.5	0.0509
9	1.399	1.377	38.8	0.0157	1.314	1.240	22.4	0.0583
10	1.410	1.396	33.6	0.0096	1.353	1.286	17.4	0.0504
11	1.372	1.363	39.5	0.0068	1.324	1.243	21.4	0.0635
12	1.412	1.386	34.3	0.0190	1.347	1.265	17.7	0.0628
13	1.363	1.329	36.6	0.0247	1.358	1.278	21.5	0.0604
14	1.428	1.427	47.3	0.0009	1.350	1.298	32.4	0.0394
15	1.376	1.373	39.9	0.0021	1.323	1.255	25.0	0.0530
16	1.454	1.450	39.7	0.0031	1.377	1.317	21.9	0.0443
Mean	1.401	1.386	37.4	0.0103	1.340	1.269	21.2	0.0546
σ	0.026	0.033	5.5	0.0098	0.021	0.027	3.9	0.0109

Table 1: The parameter outputs from the 2D Gaussian model fits are provided for both the naturally and uniformly weighted radio images. We quote the grid position, the semi-major (a) and semi-minor (b) axes, the position angle (α, measured in degrees North of East) and the ellipticity modulus ($\boldsymbol{e}$). The bottom two rows report the mean and standard deviation (σ) for each column.

Figure 3 displays the weighted mean beam shapes as measured from our simulations for the case of natural weighting (a similar equivalent can be made for the uniform weighting scheme). The best-fit parameters of the 2D elliptical Gaussian fits are provided in Table 1 for both weighting schemes. Since the effective beam size measured shows some dependency on grid position, this will be an important feature to include in our shape analysis of the real data.

3.2 Estimation of radio shapes

Having estimated the effective PSF across the image, we are now in a position to measure the shapes of those sources that are resolved by the radio observations. Here we outline our general approach to extracting source shapes. We apply this approach to the resolved sources in our simulations, and to the resolved sources in the real data, in Sections 4 and 5 respectively. When fitting for shapes, we take the source positions from Schinnerer et al. (2007) who performed their source finding with the AIPS task SAD. We then classify each source as resolved/unresolved according to an elliptical Gaussian fitting procedure. We use the CASA task IMFIT (which incorporates the deconvolution of the CLEAN beam) to fit elliptical Gaussian models to each source. We classify as resolved, those sources with a major and minor axis greater than ~ 1.2 times the effective PSF size. For the natural weighted image, we select sources according to:

$$\begin{aligned} a &> 1.8 \text{ arcseconds} \\ b &> 1.7 \text{ arcseconds} \\ S/N &> 5, \end{aligned}$$

whereas for the uniform-weighted image:

$$\begin{aligned} a &> 1.75 \text{ arcseconds} \\ b &> 1.6 \text{ arcseconds} \\ S/N &> 5, \end{aligned}$$

where a and b are the best-fit semi-major and semi-minor axes respectfully. A S/N cut of > 5 was applied, as was previously in Schinnerer et al. (2007). Since we are only concerned in position angles for this study we deem this relatively low S/N cut as sufficient to maximise source counts, although it should be noted that typical weak lensing studies would require a much larger cut and therefore reducing the sample size. After applying these cuts, we are left with 931 and 762 remaining sources in the natural and uniform weighted images respectfully.

3.2.1 Shape Estimator

In this work we make use of developments in optical shape measurement techniques. In particular, we have chosen to use the IM3SHAPE code to extract galaxy shapes, which we apply directly to our radio image. IM3SHAPE (Zuntz et al. 2013) is a maximum likelihood model-fitting algorithm for estimating galaxy ellipticities. The performance of IM3SHAPE was demonstrated, for example, during the GREAT10 optical weak lensing challenge (Kitching et al. 2012), where it achieved relatively accurate and unbiased shape measurements (Kacprzak et al. 2012).

We parametrise individual galaxy shapes in terms of a two-component ellipticity, $\boldsymbol{e} = (e_1, e_2)$. Here e_1 describes elongations parallel and perpendicular to an arbitrarily chosen reference axis and e_2 describes elongations along the

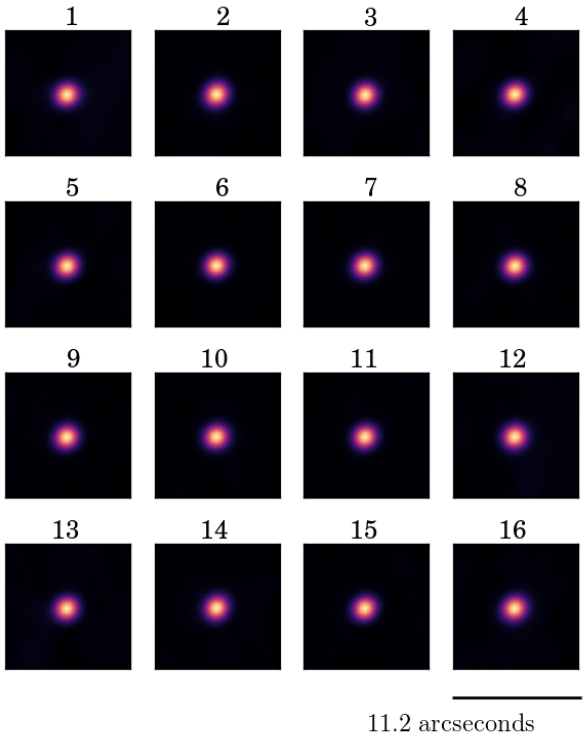

Figure 3. The spatially-dependent PSF of the VLA-COSMOS image as estimated from our simulated datasets. The full VLA-COSMOS field was split into 16 equal-size regions and the images show the average PSF within each section. This figure shows the PSF corresponding to the naturally-weighted image – the PSF corresponding to the uniformly-weighted image is broadly similar. These mean recovered PSFs are subsequently fitted with an elliptical Gaussian model to provide an effective PSF model for each region on the radio mosaic. The grid numbers shown in bold black above each cutout correspond to the grid numbers reported in Table 1. Each plot shares a linear colour scale

directions rotated $\pm 45^\circ$ from the reference axis. This ellipticity can also be expressed in terms of a semi-major (a) and semi-minor (b) axis, and a position angle (α). The ellipticity modulus $e = |\boldsymbol{e}|$ is given by

$$e = \frac{a^2 - b^2}{a^2 + b^2} = \sqrt{e_1^2 + e_2^2}, \tag{2}$$

where e_1 and e_2 are the vector elements of e,

$$e_i = \begin{pmatrix} |\boldsymbol{e}| \ \cos(2\alpha) \\ |\boldsymbol{e}| \ \sin(2\alpha) \end{pmatrix}, \tag{3}$$

and where α is the position angle,

$$\alpha = \frac{1}{2} \tan^{-1} \left(\frac{e_2}{e_1} \right). \tag{4}$$

In our shape measurement analysis, we used IM3SHAPE to fit a sum of two Sèrsic profiles, specifically a "Bulge plus Disc" model. We emphasise that the IM3SHAPE fitting procedure fully accounts for the PSF (which the user must supply) by including it in the forward model. A Sèrsic profile is a surface brightness distribution model described by,

$$I(r) = I(0) \exp \left[- \left(\frac{r}{r_0} \right)^{\frac{1}{n}} \right], \tag{5}$$

where $I(0)$ is the central intensity, r is the projected radius, r_0 is the and scale length of the profile and n is the Sèrsic index (Trujillo et al. 2001). The maximum likelihood approach optimises the model parameters by minimising the summation of the square differences between the model and the data with each iteration, i.e. it minimises the χ^2 misfit statistic.

We provide IM3SHAPE with galaxy positions (from the Schinnerer et al. 2007 source catalogue) and PSF models at each of those positions (approximated by the 16 PSF models derived from simulations, see section 3.1). IM3SHAPE preforms a fit for source parameters describing the position and shape of the galaxy in terms of the two-component Sèrsic Bulge + Disc model. Although it increases the computational time from the default IM3SHAPE settings, we choose to keep both the Disc and Bulge components of the galaxy models' Sèrsic index free. This is motivated in part since our sample is sufficiently small that this addition of computation time is not problematic. Moreover the standard Sèrsic profile, which is well tested in comparison to real optical galaxies lacks the same test in comparison to galaxies as observed in the radio. By leaving the two indices free we allow for a larger range of models. This shape measurement procedure is performed for the entire galaxy population, and for the two weighting schemes that we have implemented.

	Parameter	m	c
Natural Weighting	e_1	0.207 ± 0.042	-0.001 ± 0.011
	e_2	0.208 ± 0.035	-0.012 ± 0.008
	$\alpha^{\rm raw}$	-0.0022 ± 0.0116	-0.0099 ± 0.0080
	$\alpha^{\rm corr}$	0.0115 ± 0.0116	-0.0118 ± 0.0079
Uniform Weighting	e_1	0.125 ± 0.039	0.181 ± 0.010
	e_2	0.373 ± 0.032	-0.021 ± 0.008
	$\alpha^{\rm raw}$	-0.0870 ± 0.0081	-0.0058 ± 0.0056
	$\alpha^{\rm corr}$	0.0247 ± 0.0096	0.0120 ± 0.0066

Table 2: Best-fitting bias parameters for ellipticity components (e_1 and e_2), and for both the raw and corrected position angle components ($\alpha^{\rm raw}$ and $\alpha^{\rm corr}$; see text in Section 4.1) as measured from simulations. The measured ellipticity and position angle components are fit to a linear bias model with multiplicative (m) and additive (c) bias parameters. $\alpha^{\rm raw}$ refers to position angles estimated from the measured ellipticities using Equation (7). $\alpha^{\rm corr}$ refers to position angles estimated from ellipticities which have already been corrected for the measured e_i biases.

4 QUALITY OF SHAPE MEASUREMENTS FROM SIMULATIONS

In this section, we use the simulations described in Section 3.1 to quantify how well the galaxy shape measurement pipeline of Section 3.2 can recover the input ellipticities.

4.1 Estimation of measurement bias

4.1.1 Ellipticity measurement bias

To process our simulations, we mirror the analysis performed on the real VLA COSMOS data, producing a recovered image from the simulated visibilities using the CLEAN algorithm as described in Section 2.1.2, and measuring the shapes of the galaxies from the recovered image using IM3SHAPE.

We quantify the success of the shape recovery from the simulations in terms of a linear bias model. This is parametrised for each ellipticity component separately as,

$$e^{\rm obs} = (1+m)e^{\rm true} + c, \tag{6}$$

where m is a multiplicative, and c an additive, bias.

Figure 4 shows the recovery of the input e_1 and e_2 values for both weighting choices in the imaging algorithm, with the best-fitting multiplicative and additive bias parameters listed in Table 2. For the natural weighting scheme we find a relatively small additive bias and the multiplicative bias appears highly similar between the two ellipticity components. However, this is not true for the uniform weighting scheme, which displays a more significant additive systematic effect and a clear discrepancy in the multiplicative bias components.

4.1.2 Position angle measurement bias

In addition to measuring the accuracy of the ellipticity reconstruction, we have also assessed the accuracy with which the galaxy position angles can be reconstructed. The position angle of a galaxy can be estimated from measurements of its ellipticity components as,

$$\alpha^{\rm obs} = \frac{1}{2}\tan^{-1}\left(\frac{e_2^{\rm obs}}{e_1^{\rm obs}}\right). \tag{7}$$

From Equation (6) it is clear that, for a small additive ellipticity bias and highly similar multiplicative ellipticity biases, position angle estimates based on Equation (7) should be relatively unbiased. We therefore expect to recover relatively unbiased position angle estimates from our naturally weighted images for which we found small additive ellipticity biases and highly similar multiplicative biases.

Figure 5 shows the position angles $\alpha^{\rm obs}$, recovered from the source ellipticities measured in our simulations. In addition to the "raw" position angles $\alpha^{\rm raw}$ we have also estimated the position angles from ellipticity measurements which have already been debiased using the best-fitting linear ellipticity bias model parameters. We label these corrected position angle measurements $\alpha^{\rm corr}$. We fit a linear bias model to both the $\alpha^{\rm raw}$ and $\alpha^{\rm corr}$ estimates (as a function of the true position angles $\alpha^{\rm true}$). Figure 5 shows that the extracted position angles using the natural weighting scheme are essentially unbiased, both before and after correction for the measured ellipticity bias, although they are still a noisy estimate. The same is not true for the uniform weighting scheme where a residual multiplicative bias remains. Based on these results, we choose the natural weighting scheme for the remainder of this work. Note that although we have used a simple linear model for the bias in α, this may not necessarily be a good model in the limit of very precise measurements. However, it appears to provide a good approximation given the level of measurement noise present here. The best-fitting parameters for this linear model are listed in Table 2. The associated uncertainties from values in Table 2 were obtained from the covariance matrix of the linear model fit.

In Appendix A we investigate how the a position angle recovery obtained may relate to requirements on shear additive and multiplicative systematics in current and future optical weak lensing surveys. Figure 6 demonstrates the shear recovery achievable using a position angle-only shear estimators (as detailed in Whittaker et al. (2014)). For comparison we have over-plotted with the white error bar the approximate results obtained in from simulations in this study, additionally we show weak lensing requirements with optical studies with the black contours. We can see here that although our position angle estimates are relatively unbiased within measurement errors, the resultant uncertainty on the position angle bias parameters from this study is large compared to current capabilities. For more information on Figure 6 see Appendix A.

5 RADIO SHAPE MEASUREMENTS WITH DATA

For the radio images we have constructed from the real data (with the pipeline described in Section 2.1.2), we measure source ellipticities with IM3SHAPE, with the application of simulated effective PSF models approximated over the field (see Section 3.1). We convert these ellipticity measurements to position angle estimates, α using Equation (4) to create

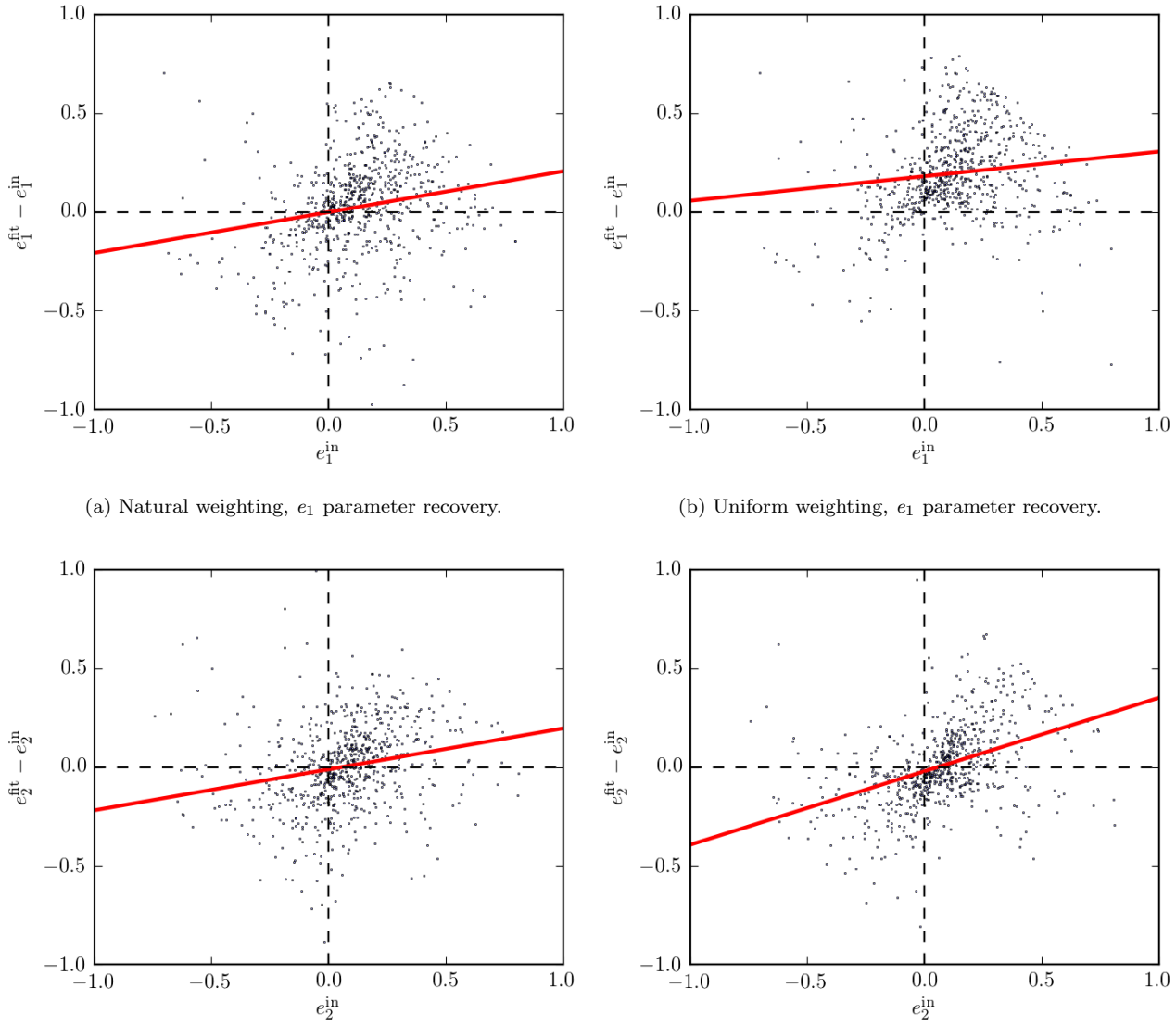

(a) Natural weighting, e_1 parameter recovery.

(b) Uniform weighting, e_1 parameter recovery.

(c) Natural weighting, e_2 parameter recovery.

(d) Uniform weighting, e_2 parameter recovery.

Figure 4. Shape parameter recovery from simulations. The figures show the residuals in the ellipticity components as measured from the simulated radio datasets. Each point represents the measurements for a single galaxy. Panels (a) & (c) show the recovery of e_1 and e_2 from images produced using natural weighting. Panels (b) & (d) show the same for images produced using uniform weighting. In each panel, a regression line is overplotted using the best fitting parameters reported in Table 2.

the full galaxy morphology catalogue[8]. Note that the e_i components are corrected for multiplicative and additive bias, as estimated from the corresponding simulations, following Equation (6). However, this has little effect on the resulting α values for the image created with natural weighting (see discussion in Section 4).

As a measure of the improvement in our VLA COSMOS imaging (from the point of view of shape estimation) over the original analysis of Schinnerer et al. (2007), in Figure 7 we compare histograms of the measured position angles from the two analyses. The figure reveals a large discrepancy in the distributions measured from the two images, with the position angles extracted from our new image being distributed much closer to the uniform distribution expected for such a large sample. The large systematic correlations in position angles present in the original image would clearly pose a problem for any subsequent analyses which rely on accurate measurements of galaxy shapes.

We compare the distribution of the galaxy ellipticity moduli, $|\boldsymbol{e}|$, measured from our new VLA COSMOS image, to a model distribution in Figure 9. The model we compare to is a reasonable approximation of a typical optical shape distribution, and is taken from the GRavitational lEnsing Accuracy Testing 2008 (GREAT08) analysis (Bridle et al. 2010). The functional form is given by

$$P(|\boldsymbol{e}|) = |\boldsymbol{e}| \left[\cos\left(\frac{\pi|\boldsymbol{e}|}{2}\right)\right]^2 \exp\left[-\left(\frac{2|\boldsymbol{e}|}{B}\right)^C\right], \quad (8)$$

[8] A source catalogue can be found at `https://github.com/bentunbridge/cosmos-radio-optical`.

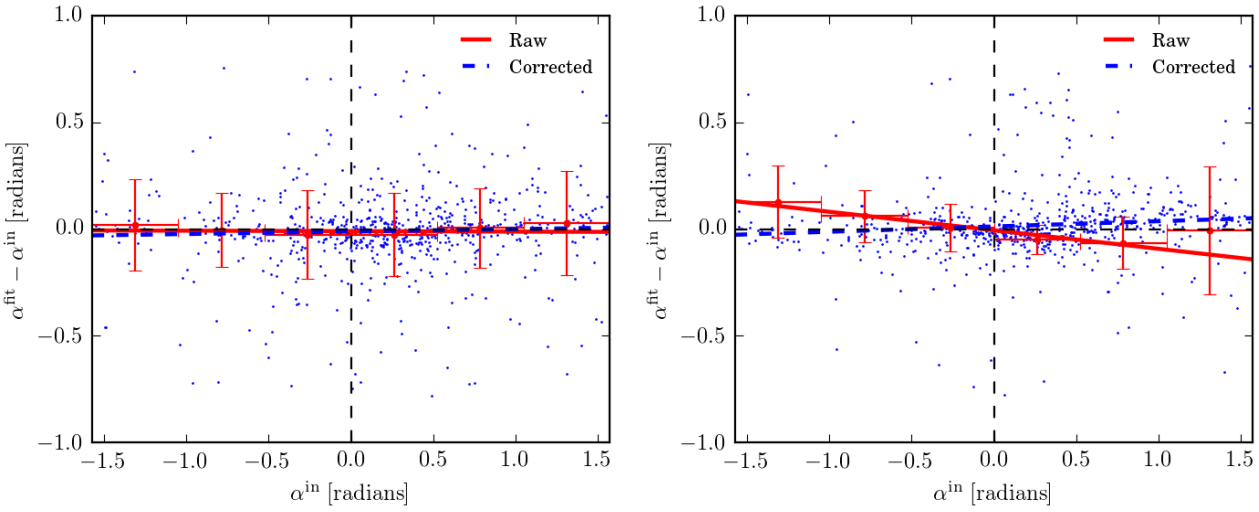

(a) Natural weighting, α parameter recovery.

(b) Uniform weighting, α parameter recovery.

Figure 5. Residuals in the recovery of the galaxy position angles (α) for both weighting schemes considered (*left*: natural weighting, *right*: uniform weighting). The points show the bias corrected points while the binned error bars show the distribution before bias correction. In addition to the "raw" position angle estimates, the figure also shows the result for the bias-corrected measurements as described in Appendix A. For each analysis, a regression line is over-plot: red (solid) and blue (dashed) lines show the regression line fits before and after bias corrections respectfully.

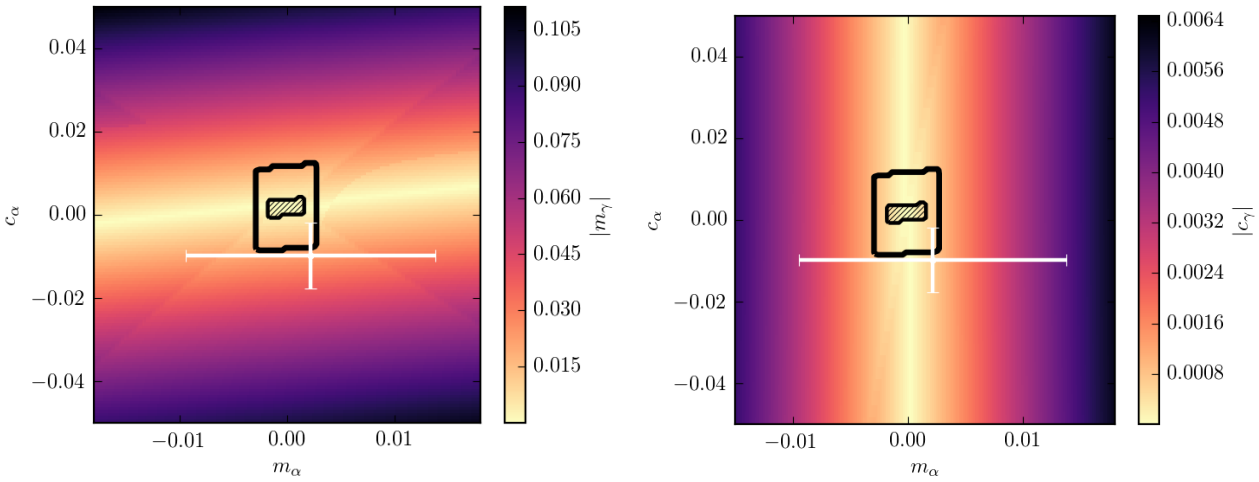

(a) Absolute m_γ colour scale.

(b) Absolute c_γ colour scale.

Figure 6. Relation between position angle bias and lensing shear bias as derived from simulations. The colour scale shows the level of multiplicative shear bias ($|m_\gamma|$, *left panel*) and additive shear bias ($|c_\gamma|$, *right panel*) as a function of the position angle bias (m_α and c_α) injected into the simulations. For comparison, the requirements on m_γ and c_γ for Stage II and Stage III surveys from Table 5 are shown as the area enclosed by the outer and inner contours respectively. The performance of our position angle estimator, as derived from the VLA-COSMOS simulations of Section 4.1, is over-plotted in each panel as a single point with error bars. For further detail see Appendix A.

where parameters, $B = 0.19$ and $C = 0.58$ are appropriate for disc-dominated galaxies. We find that the $|\boldsymbol{e}|$ distribution measured from the radio data is slightly broader than that expected for an optical sample. This may be a genuine feature of the shape population or a possible effect in the radio imaging that has not been accounted for. We measure an ellipticity dispersion of $\sigma_e = 0.29$ (per ellipticity component) and best-fitting model parameter values of $\mathrm{B} = 0.113 \pm 0.041$ and $\mathrm{C} = 0.303 \pm 0.058$ in Equation (8). In Figure 9, we also show the distribution recovered from our analysis of the HST optical data (see next Section), finding a much better agreement with the model curve assuming the fiducial parameters (as expected). For the optical data we find best-fitting model parameter values of $B = 4.65 \pm 0.288 \times 10^{-5}$ and $C = 0.218 \pm 0.002$.

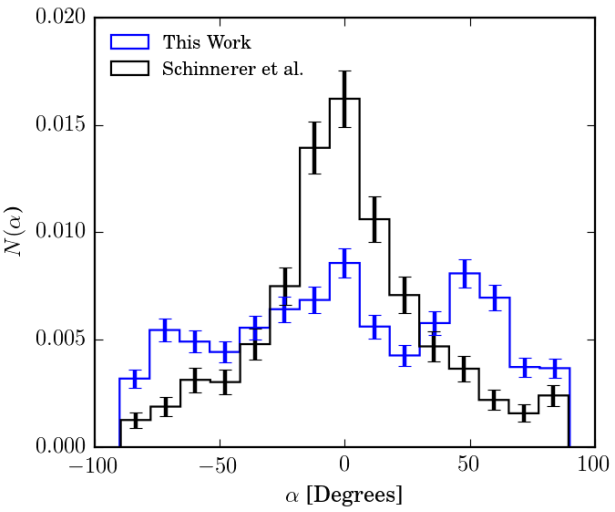

Figure 7. Normalised distribution of source position angles, α, as estimated from two independent imaging analyses of the VLA COSMOS data. The black points show the distribution based on the image produced by Schinnerer et al. (2007), while the blue points show the distribution from the image created in this work using natural weighting. Poisson error bars are included.

6 MULTI-WAVEBAND SHAPE COMPARISON

Weak lensing at radio wavelengths can provide an important complementary study to equivalent studies at optical wavelengths. An important aspect of such complementarity is how radio and optical galaxy shapes intrinsically relate to each other. This has important implications for how a radio weak lensing survey may be used in synergy with overlapping optical observations. For example if radio and optical shapes are typically intrinsically aligned then the radio provides an alternative measure, with different systematics, but probing the same weak lensing sample as the optical observations. On the other hand if radio and optical shapes are intrinsically uncorrelated then the radio effectively probes a different sample of galaxies, at the same redshifts as the optical catalogue, but again with different systematics. In Figure 5 we demonstrated that our position angle estimator, though noisy, provided unbiased measurements of the galaxy position angles from the simulated radio datasets. We therefore conduct our galaxy shape comparative study in the COSMOS field using galaxy position angle measurements.

6.1 Optical shape measurement

We measured the shapes of galaxies in the optical from the HST-ACS data described previously in Section 2.2. The high density of sources in the HST image allows for PSF models to be created from the sample of stars detected across each CCD tile exposure. Stars, unlike galaxies, should be intrinsically point-like, and so can be used to estimate the PSF over the observed field. For this task we use the PSFEx ('PSF Extractor') software (Bertin 2011) which has been used in previous optical weak lensing studies (e.g. Jarvis et al. 2015).

To apply PSFEx to the HST data, we follow the pipeline used for the weak lensing analysis of the DES data (Jarvis et al. 2015), which we summarize here.

(i) We create a source catalogue with the source extraction software, SExtractor (Bertin & Arnouts 1996). We do this individually for each observation pointing with the aid of a corresponding RMS noise map for the observation. For these observations, the F814W magnitude zero-point is set to 27.2 to match the limiting point-source depth achieved in the observations (Koekemoer et al. 2007).

(ii) A catalogue of stars is required for each field in order to form PSFEx models. For the first iteration of the models, we apply a selection cut of CLASS_STAR > 0.6 to the catalogues produced in (i), where CLASS_STAR is a star/galaxy classification parameter and described in more detail in Bertin & Arnouts (1996). Additionally only stars with $S/N > 20$ are considered in this sample. This provides us with a sample that is mostly composed of stars and point-like objects, and serves as a rough basis to form PSFEx models. The reliability of CLASS_STAR is discussed in Holwerda (2005).

(iii) We conduct a second iteration of star classification on the data. Once again we use SExtractor to produce a source catalogue, where the software is now provided with the PSF models produced in step (ii) with PSFEx. For this iteration, the software incorporates the PSF model into the extracted parameters and we are able to produce a more reliable star/galaxy classification. We adapt the pseudo-code detailed in Jarvis et al. (2015) for our own star source selection which we implement as follows:

BRIGHT_TEST = CLASS_STAR > 0.6
AND MAG_AUTO < 25.0

LOCUS_TEST = SPREAD_MODEL
+SPREADERR_MODEL < 0.003

FAINT_PSF_TEST = MAG_PSF > 40.0
AND MAG_AUTO < 26.0
AND MAG_PSF < 90.0

GALAXIES = NOT BRIGHT_TEST
AND NOT LOCUS_TEST
AND NOT FAINT_PSF_TEST

STARS = [LOCUS_TEST OR BRIGHT_TEST]
AND NOT FAINT_PSF_TEST

Sources are only included in our star sample if they are identified by the BRIGHT_TEST or LOCUS_TEST and if they are not removed as junk in the FAINT_PSF_TEST. Here the BRIGHT_TEST procedure simply relies on SExtractor's own source classification system, this time excluding bright sources (Magnitude > 25) from the sample. The LOCUS_TEST procedure identifies the sourc locations relative to the stellar locus via the SPREAD_MODEL parameter. This is an additional star/galaxy classifier based on the linear discriminant between the best fitting PSF model (from step (ii)) and a model made from the same PSF convolved with a circular exponential disc model (see Desai et al. 2012, for a more detailed discussion on the SPREAD_MODEL classifier). Again we only include stars with $S/N > 20$ in our final stellar sample.

(iv) Finally we again generate PSF models, this time from

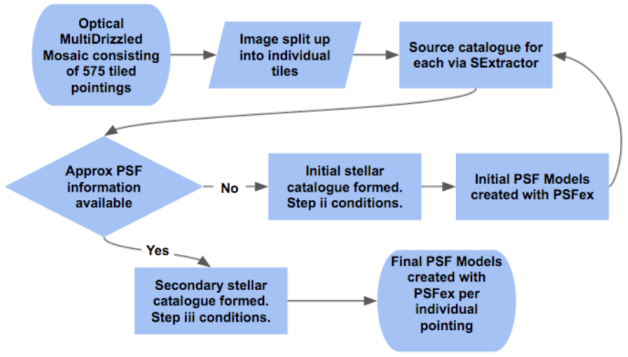
Optical MultiDrizzled Mosaic consisting of 575 tiled pointings
Image split up into individual tiles
Source catalogue for each via SExtractor
Approx PSF information available
No
Initial stellar catalogue formed. Step ii conditions.
Initial PSF Models created with PSFex
Yes
Secondary stellar catalogue formed. Step iii conditions.
Final PSF Models created with PSFex per individual pointing

Figure 8. A flow chart depicting the optical PSF modelling pipeline. Each of the 575 pointings are first run through SExtractor and PSFex to form PSF models with an initial stellar population estimate. Following this an improved stellar population is extracted and subsequently improved PSFex models are generated.

Study	σ_e	B	C
STEP	0.3	0.19	0.58
Optical	0.26	$4.65 \pm 0.288 \times 10^{-5}$	0.218 ± 0.002
Radio	0.29	0.137 ± 0.024	0.318 ± 0.032

Table 3: Comparison of the measured ellipticity dispersion and ellipticity distribution fit parameters for the radio and optical datasets. Also listed are the parameters adopted for the representative model used in the GREAT08 analysis of Bridle et al. (2010).

the improved stellar sample from step (iii) and using PSFex. This provides a PSF model as a function of position on the sky for each of the 575 pointings across the entire mosaic, which we will use for shape analysis.

These steps are depicted as a flowchart in Figure 8.

Having constructed PSF models, we then proceed to measure the shapes of galaxies in the HST-ACS data. For this we make use of previous work by McCracken et al. (2010) to serve as our source position catalogue. This analysis provides a photometric catalogue containing 438,226 sources with a source number density of $\sim$ 74 arcmin^{-2} in the 2 deg^2 field, far surpassing the radio source density of 0.14 arcmin^{-2}. The catalogue was extracted using SExtractor; for a detailed description see McCracken et al. (2010).

For each galaxy in this catalogue, we measure the optical source shape with im3shape, making use of the PSF models described above. The resulting optical shape catalogue can be found at `https://github.com/bentunbridge/cosmos-radio-optical`. Once again, we refer the reader to Figure 9 which compares the ellipticity distributions as measured in the optical and in the radio. For the optical data, we measure $\sigma_e = 0.26$ per ellipticity component with a model fit of $B = 4.65 \pm 0.288 \times 10^{-5}$ and $C = 0.218 \pm 0.002$. The fitted parameters for both radio and optical ellipticity distributions are summarised in Table 3.

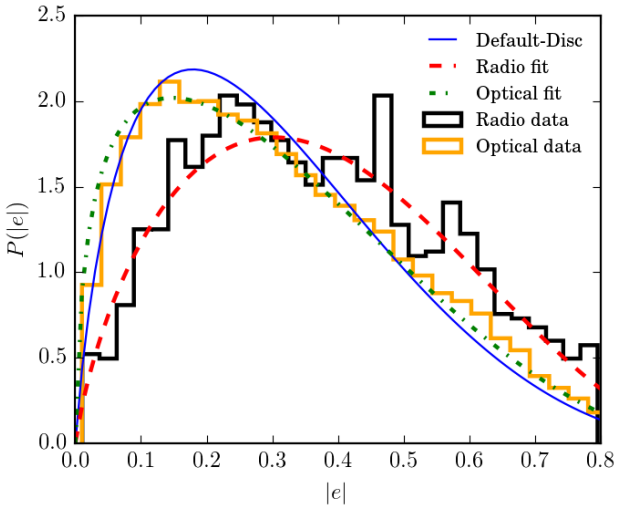

Figure 9. Galaxy ellipticity distributions measured from the radio and optical COSMOS data. An ellipticity distribution model appropriate for disk galaxies (Equation (8)) is shown in blue, for model parameters $B = 0.19$ and $C = 0.58$. The VLA COSMOS galaxy $|\boldsymbol{e}|$ measurements are shown as the black histogram which is best-fitted by Equation (8) using B and C values of 0.113 ± 0.041 and 0.303 ± 0.058 respectively (shown as the red dotted line). The ellipticity distribution as measured from the HST optical data (shown as the orange histogram) is best-fit with model parameters $B = 4.65 \pm 0.288 \times 10^{-5}$ and $C = 0.218 \pm 0.002$ (shown as the green dash-dot line).

6.2 Radio-optical shape correlations

With possession of shape measurements in both the optical and radio observations, we perform a cross-wavelength comparison of the source position angles. Motivated by the simulation results of Section 4 we perform the comparison with the position angle estimates, also noting the existence of shear estimators which make use of position angles (Whittaker et al. 2014). We make individual cut-out images comparing the source shapes in radio and optical available at `https://github.com/bentunbridge/cosmos-radio-optical` – we show a selection of these in Figure 10.

To aid a statistical comparsion, we also compute the associated uncertainties in the position angle measurements, σ_α, for both the radio and optical shape catalogues. For the radio catalogue, the scatter in the position angles estimated from the VLA-COSMOS simulations (see Section 4) are used to estimate σ_α as a function of S/N. For the optical measurements we take advantage of previous work to estimate the uncertainty in an image-plane ellipticity measurement for a source with a given S/N in the case of un-correlated pixel noise. The statistical uncertainties were derived analytically by Kacprzak et al. (2012) and Refregier et al. (2012) who also demonstrated the validity of these expressions using simplified galaxy models including multiplicative and additive noise with the im3shape code. For ellipticity components this uncertainty estimate is given by,

$$\sigma_{e_i} = \frac{(1 - e_i^2)}{S/N}, \qquad (9)$$

where S/N is the ideal estimate of the signal-to-noise of the

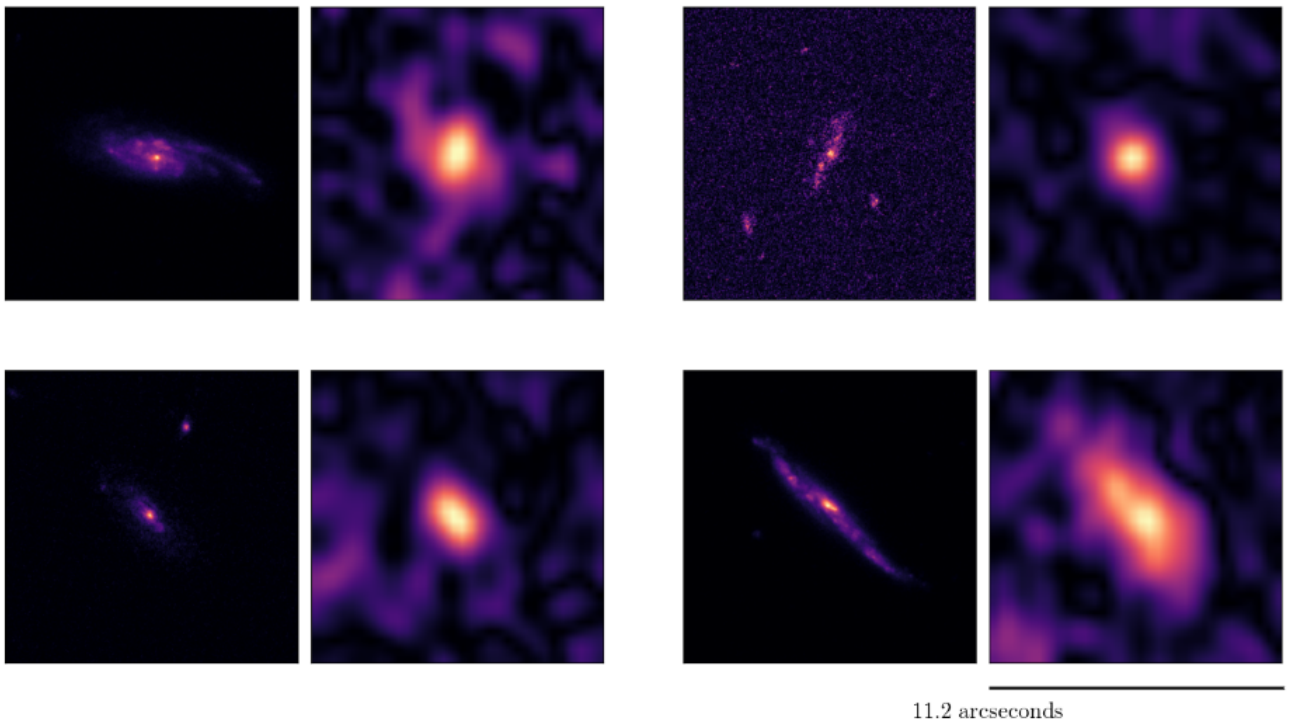

Figure 10. Comparison between the radio and optical images for 4 sources in the catalogue. In each case a $11.2'' \times 11.2''$ cutout is shown for the optical (*left panels*) and radio (*right panels*) images of the matched source. Note the much poorer resolution of the radio images.

galaxy. Note that for nearly circular sources, i.e. small e value, the statistical error associated with shape measurements saturates. Hence σ_α is derived through propagation from Equation (4).

Figure 11 shows a comparison of the average uncertainty in the position angle (σ_α) as a function of S/N for both the radio and optical bands, where for the radio we have included the uncertainties for the naturally imaged weighting scheme, as used in this study. As can be seen, at low S/N the radio position angles are estimated with a similar precision as is achieved in the optical. However the improvement seen in the α recovery at increased S/N levels in the optical is not mirrored to the same extent in the radio data.

Radio and optical sources are cross-matched to within a positional tolerance of 1.0 arcsec and the position angles of the matched sample are cross-correlated. Within the uncertainties we do not make a statistically significant detection of correlation across the sample as a whole. We measure the Pearson's correlation coefficient in α and find $R_\alpha = 0.024$ and $R_\alpha = 0.028$ for the images created using the natural weighting respectively. These low values of R_α indicate a clear lack of correlation between the data sets (a strong positive correlation would give $R_\alpha = 1$).

Although we do not detect a correlation in the radio and optical shapes, we investigate further in order to place limits on a global physical correlation. Assuming that optical and radio galaxy position angles do have some association, we may place limits on the level of astrophysical scatter ($\sigma_\alpha^{\rm scatter}$) required to produce the observed lack of correlation, taking into account our measurement errors. To do this, we conduct Monte Carlo (MC) simulations of catalogues of radio and optical matched objects. Taking into account the measurement errors, we incrementally increase the level of astrophysical scatter between the simulated ra-

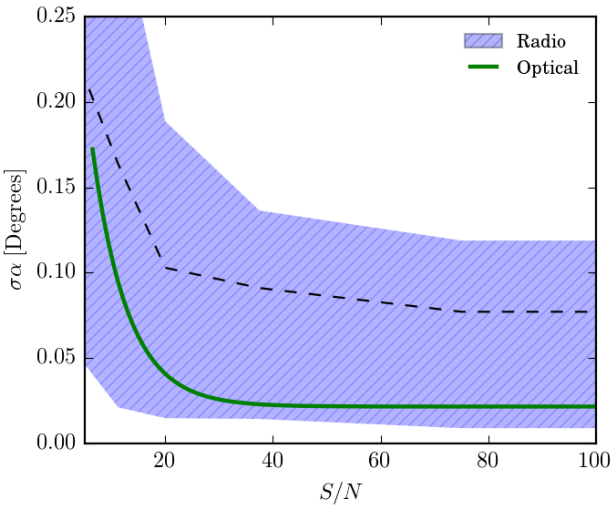

Figure 11. Average uncertainty in position angle measurements for both the radio and optical samples as a function of S/N. Radio uncertainties for the natural weighting scheme is derived from simulations and shown by the dashed line for our sample of radio galaxies. The hatched area shows this to a confidence level of 68%. The optical uncertainties are calculated analytically following Refregier et al. (2012).

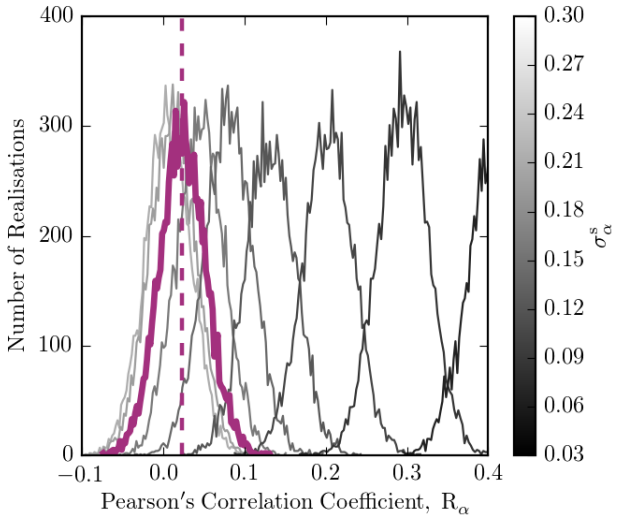

Figure 12. Comparison of the distribution of Pearson correlation coefficients (R_α) measured from simulations of matched catalogues for varying levels of intrinsic (astrophysical) scatter in the radio-optical position angle correlation as detailed by the colour scale ($\sigma^s_\alpha = \sigma^{\rm scatter}_\alpha/\pi$). The vertical dashed line shows the corresponding measurement from the data (≈ 0.24). For comparison we highlight the most consistent histogram, shown by the bold purple histogram.

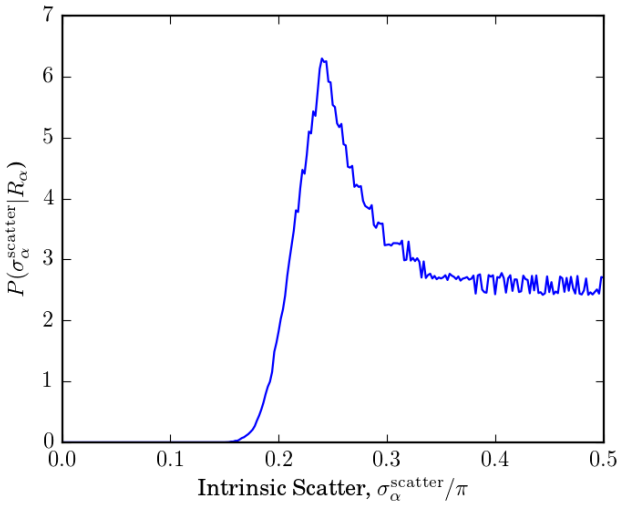

Figure 13. Limits on the intrinsic (astrophysical) scatter between the position angles of the same galaxies in the radio and optical bands. The curves show $P(\sigma^{\rm scatter}_\alpha|R_\alpha)$ – the probability distribution of $\sigma^{\rm scatter}_\alpha$ given the measured value of R_α. The results obtained using the natural weighted radio image is shown as the blue curve.

dio and optical shapes, each time computing the R_α value for 10,000 realisations. The results are shown in Figure 12 where we also compare to the R_α value measured from the real data. We emphasise that our MC simulations fully capture both the shape measurement errors and the statistical error due to the finite number of sources in the data.

The results are further summarised in Figure 13 where we plot $P(\sigma^{\rm scatter}_\alpha|R_\alpha)$: the probability distribution of $\sigma^{\rm scatter}_\alpha$ given the value of R_α measured from the data. The measured R_α is shown to be most consistent with a $\sigma^{\rm scatter}_\alpha$ value of 0.24π radians (or 14.3°) and the distribution corresponds to a 95% lower limit of 0.212π radians (or 38.2°) on $\sigma^{\rm scatter}_\alpha$.

6.3 Relation to earlier results

Although the shapes of galaxies as measured in the optical and radio need not necessarily be aligned, previous studies have suggested such an alignment, at least for certain galaxy types. In particular, Battye & Browne (2009) were able to show a strong alignment of the radio and optical images of galaxies classified as late-type and a weaker *anti*-alignment correlation in position angle for sources classified as early-type galaxies. A physical motivation for this pattern can be made from the source of radio emission in each case. For late-type galaxies, radio emission is related to areas of recent star formation and so is expected to trace the similarly generated optical emission. In early-type galaxies the radio emission is driven by accretion on to a central black hole, producing bright jets anti-aligned with the galaxy disc, causing radio emission to be aligned with the optical minor axis. Battye & Browne (2009) made use of the Sloan Digital Sky Survey (SDSS) and the Faint Images of the Radio Sky at Twenty centimetres (FIRST) for the optical and radio observations respectively. The key difference with the work presented here is the comparatively large volumes probed by SDSS and FIRST, compared to COSMOS. Between SDSS and FIRST 239,993 matches are made between the optical and radio observations (although this is before the application of any selection cuts), far surpassing the 761 sources used in this study.

In order to make a comparison between the studies, we implemented similar selection cuts to those used by Battye & Browne (2009). Their cuts included only considering bright sources via a Magnitude cut-off $M > 18$, and a limitation on the ellipticity, implemented as $b/a < 0.8$ (where a and b are the semi-major and semi-minor axis respectively), for both the optical (SDSS) and radio (FIRST) sample. Finally, a cut on the minimum radio source size was applied ($a > 2''$) resulting in a sample of 14302 galaxies. We modify these cuts due to the differences in the observation properties. In particular, we choose not to implement a magnitude cut since we have already applied S/N cuts ($S/N > 10$ and $S/N > 5$ for the optical and radio samples respectively). We impose the same cuts on ellipticity, only including sources with $b/a < 0.8$ in both the optical (HST-ACS) and radio (VLA) samples. We impose a less stringent size cut ($a > 1''$) compared to that used in Battye & Browne (2009) due to the increased resolution of the COSMOS data.[9]

After implemented these cuts, only 327 sources remain. Of these 327, we can further split the sample into galaxy morphology types by matching to a previous COSMOS morphology catalogue compiled by Scarlata et al. (2006). The results are summarised in Table 4. Correlating the radio and optical shapes within these classification subsets, we again find no meaningful correlation between the radio and optical

[9] The FIRST data used in Battye & Browne (2009) has a resolution of $5''$, compared to $\sim 1.5''$ for the VLA-COSMOS data.

Type	Number	Fraction
Early	59	0.18
Late	120	0.37
Irregular	122	0.37
No Classification	26	0.08

Table 4: Sub-samples of the COSMOS radio-optical matched catalogue, after undergoing further selection cuts, and subdivided according to galaxy type. From the full sample of radio galaxies detected in our VLA-COSMOS image we find 761 galaxies are successfully matched to an optical source. However only 327 remain after the applying the cuts described in Section 6.3.

shapes. We note however that the number of galaxies in our sub-samples are small. We further note that the main sample of galaxies used in this study (being composed mainly of faint, high-redshift star-forming galaxies) will be a much closer match to a typical weak lensing galaxy sample, compared to the sample identified in Battye & Browne (2009).

An apparent lack of correlation between optical and radio galaxy shapes has been commented on before by Patel et al. (2010). This study attempted to measure a weak lensing signal in the radio with eMERLIN and VLA observations, while simultaneously conducting a cross correlations study of galaxy shapes. Subsequently they found no correlation between the optical and radio shapes, which is consistent with our findings here.

7 CONCLUSIONS

In this paper we have performed a detailed comparison analysis of the shapes of galaxies in the COSMOS field, as measured in the optical using HST, and as measured in the radio, using the VLA. Our study has been motivated by the scientific potential of cross-correlation cosmic shear analyses of future overlapping optical and radio surveys (Brown et al. 2015; Harrison et al. 2016; Bonaldi et al. 2016; Camera et al. 2016). In order to fully exploit such future cross-correlations, one needs to understand in detail the correlations in intrinsic optical and radio shapes, which is the issue that we have attempted to address in this study.

In the course of our analysis, we have highlighted some of the challenges involved in extracting shapes from radio observations. For this analysis we have chosen to measure galaxy shapes from images reconstructed from the VLA radio data. In particular, we have used simulations, composed of a known distribution of galaxy shapes combined with a realistic radio interferometer observation and imaging pipeline, to show the effectiveness of position angle (α) recovery through typical radio data reduction and image creation techniques. We have investigated the use of two variations of the widely used Högbom-CLEAN image creation algorithm in the radio: natural and uniform visibility weighting. We find the choice in weighting scheme affects the measured shape parameters greatly. In particular the choice of a uniform weighting scheme yields largely discrepant values of multiplicative bias in ellipticity components for a given galaxy. We found this problem was diminished when natural weighting was used, which produced highly similar multiplicative bias on ellipticities, which later cancels when position angles are derived from the measured ellipticities. This allowed us to obtain unbiased estimates of the position angles, which were important for this study.

Quantifying the bias in position angle (α) achieved in this study with a linear bias model, a link to weak lensing requirements for future surveys was established via the position angle only shear estimators of Whittaker et al. (2014). A key result is shown in Figure 6 which allows one to translate from the usually quoted requirements on shear bias to requirements on position-angle bias. We find that although our position angle recovery appears relatively unbiased given our measurement errors, the uncertainty on the position angle bias that we are able to achieve using current data is still larger than current weak lensing requirements.

After quantifying the expected uncertainties through simulations we have applied our shape measurement pipeline to the real COSMOS radio (VLA) observations. We used the resulting radio galaxy shape measurements (and associated uncertainties) to place a lower limit on the astrophysical scatter in source position angles between the continuum radio and optical emission of the sources which are detected in both our VLA data and an optical HST study of the same field. We find this lower limit to be $\sigma_{\alpha}^{\rm scatter} \gtrsim 0.212\pi$ (or 38.2°) at a 95% confidence level. This appears consistent with results from previous studies (Patel et al. 2010) considering the low absolute number of sources in our sample.

Understanding the radio-optical shape correlations is important as it will affect the noise term on the cosmological power spectra measured by radio-optical cross-correlation weak lensing studies (Harrison et al. 2016; Camera et al. 2016). High levels of correlation will increase the shot noise on shear measurement, but allow for cross-waveband calibration against some systematics, whilst low levels of correlation effectively increase the source number density being used to probe the cosmic shear field. In the near future deep, high-resolution optical and radio surveys such as SuperCLASS[10] will further constrain this correlation, better informing forecasts and survey design considerations for SKA.

ACKNOWLEDGEMENTS

We thank Chris Hales, Anita Richards, Neal Jackson, Lee Whittaker and Joe Zuntz for useful discussions. We further thank Chris Hales, Eva Schinnerer and Vernesa Smolcic for providing us with the partially processed VLA data. MLB is an STFC Advanced/Halliday fellow. BT, IH and MLB are supported by an ERC Starting Grant (grant no. 280127).

REFERENCES

Amara, A., Réfrégier, A., 2008, MNRAS, 391, 228, arXiv:0710.5171

Battye, R. A., Browne, I. W. A., 2009, MNRAS, 399, 1888, arXiv:0902.1631

[10] `http://www.e-merlin.ac.uk/legacy/projects/superclass.html`

Becker, R. H., White, R. L., Helfand, D. J., 1995, ApJ, 450, 559
Bertin, E., 2011, in Astronomical Data Analysis Software and Systems XX, edited by Evans, I. N., Accomazzi, A., Mink, D. J., Rots, A. H., vol. 442 of *Astronomical Society of the Pacific Conference Series*, 435
Bertin, E., Arnouts, S., 1996, A&AS, 117, 393
Bonaldi, A., Harrison, I., Camera, S., Brown, M. L., 2016, ArXiv e-prints, arXiv:1601.03948
Bridle, S., Balan, S. T., Bethge, M., et al., 2010, MNRAS, 405, 2044, arXiv:0908.0945
Brown, M., Bacon, D., Camera, S., et al., 2015, Advancing Astrophysics with the Square Kilometre Array (AASKA14), 23, arXiv:1501.03828
Brown, M. L., Battye, R. A., 2011, MNRAS, 410, 2057, arXiv:1005.1926
Camera, S., Harrison, I., Bonaldi, A., Brown, M. L., 2016, ArXiv e-prints, arXiv:1606.03451
Carozzi, T. D., Woan, G., 2009, MNRAS, 395, 1558, arXiv:0812.0141
Chang, T.-C., Refregier, A., 2002, ApJ, 570, 447, astro-ph/0107085
Chang, T.-C., Refregier, A., Helfand, D. J., 2004, ApJ, 617, 794, astro-ph/0408548
Cornwell, T. J., Golap, K., Bhatnagar, S., 2008, IEEE Journal of Selected Topics in Signal Processing, 2, 647, arXiv:0807.4161
Demetroullas, C., Brown, M. L., 2016, MNRAS, 456, 3100, arXiv:1507.05977
Desai, S., Armstrong, R., Mohr, J. J., et al., 2012, ApJ, 757, 83, arXiv:1204.1210
Fomalont, E. B., Perley, R. A., 1999, in Synthesis Imaging in Radio Astronomy II, edited by Taylor, G. B., Carilli, C. L., Perley, R. A., vol. 180 of *Astronomical Society of the Pacific Conference Series*, 79
Harrison, I., Camera, S., Zuntz, J., Brown, M. L., 2016, ArXiv e-prints, arXiv:1601.03947
Högbom, J. A., 1974, A&AS, 15, 417
Holwerda, B. W., 2005, ArXiv Astrophysics e-prints, astro-ph/0512139
Jarvis, M., Sheldon, E., Zuntz, J., et al., 2015, ArXiv e-prints, arXiv:1507.05603
Jee, M. J., Tyson, J. A., Hilbert, S., Schneider, M. D., Schmidt, S., Wittman, D., 2015, ArXiv e-prints, arXiv:1510.03962
Kacprzak, T., Zuntz, J., Rowe, B., et al., 2012, MNRAS, 427, 2711, arXiv:1203.5049
Kilbinger, M., 2015, Reports on Progress in Physics, 78, 8, 086901, arXiv:1411.0115
Kitching, T. D., Balan, S. T., Bridle, S., et al., 2012, MNRAS, 423, 3163, arXiv:1202.5254
Koekemoer, A. M., Aussel, H., Calzetti, D., et al., 2007, ApJS, 172, 196, astro-ph/0703095
Koekemoer, A. M., Fruchter, A. S., Hook, R. N., Hack, W., 2003, in HST Calibration Workshop : Hubble after the Installation of the ACS and the NICMOS Cooling System, edited by Arribas, S., Koekemoer, A., Whitmore, B., 337
Köhlinger, F., Viola, M., Valkenburg, W., Joachimi, B., Hoekstra, H., Kuijken, K., 2016, MNRAS, 456, 1508, arXiv:1509.04071
McCracken, H. J., Capak, P., Salvato, M., et al., 2010, ApJ, 708, 202, arXiv:0910.2705
McMullin, J. P., Waters, B., Schiebel, D., Young, W., Golap, K., 2007, in Astronomical Data Analysis Software and Systems XVI, edited by Shaw, R. A., Hill, F., Bell, D. J., vol. 376 of *Astronomical Society of the Pacific Conference Series*, 127
Morales, M. F., 2006, ApJ, 650, L21, astro-ph/0608494
Noordam, J. E., 2004, in Ground-based Telescopes, edited by Oschmann, J. M., Jr., vol. 5489 of Proc. SPIE, 817–825
Patel, P., Bacon, D. J., Beswick, R. J., Muxlow, T. W. B., Hoyle, B., 2010, MNRAS, 401, 2572, arXiv:0907.5156
Patel, P., Harrison, I., Makhathini, S., et al., 2015, Advancing Astrophysics with the Square Kilometre Array (AASKA14), 30, arXiv:1501.03892
Refregier, A., Kacprzak, T., Amara, A., Bridle, S., Rowe, B., 2012, MNRAS, 425, 1951, arXiv:1203.5050
Rowe, B. T. P., Jarvis, M., Mandelbaum, R., et al., 2015, Astronomy and Computing, 10, 121, arXiv:1407.7676
Scarlata, C., Carollo, C. M., Lilly, S. J., et al., 2006, ArXiv Astrophysics e-prints, astro-ph/0611644
Schinnerer, E., Smolčić, V., Carilli, C. L., et al., 2007, ApJS, 172, 46, astro-ph/0612314
Taylor, G. B., Carilli, C. L., Perley, R. A., eds., 1999, Synthesis Imaging in Radio Astronomy II, vol. 180 of *Astronomical Society of the Pacific Conference Series*
The Dark Energy Survey Collaboration, Abbott, T., Abdalla, F. B., et al., 2015, ArXiv e-prints, arXiv:1507.05552
Trujillo, I., Aguerri, J. A. L., Cepa, J., Gutiérrez, C. M., 2001, MNRAS, 321, 269, astro-ph/0009097
Whittaker, L., Brown, M. L., Battye, R. A., 2014, MNRAS, 445, 1836, arXiv:1311.3926
Whittaker, L., Brown, M. L., Battye, R. A., 2015a, MNRAS, 454, 2154, arXiv:1505.08131
Whittaker, L., Brown, M. L., Battye, R. A., 2015b, MNRAS, 451, 383, arXiv:1503.00061
Zuntz, J., Kacprzak, T., Voigt, L., Hirsch, M., Rowe, B., Bridle, S., 2013, MNRAS, 434, 1604, arXiv:1302.0183

A POSITION ANGLE TO SHEAR BIAS

In this section we relate our shape recovery in terms of shear. It is important to propagate obtained bias in position angle recovery (see Section 4) to the actual quantity of interest for scientific inference: the measured shear which can be related to the line of sight gravitational potential. Requirements on shear measurement additive and multiplicative systematics for these errors to be smaller than statistical uncertainties (calculated according to the prescription derived in Amara & Réfrégier 2008) are given in Table 5.

For shear estimation from ellipticities using the naïve estimator,

$$\hat{\gamma} = \frac{1}{N}\sum_{i=1}^{N} e_i^{\rm obs}, \tag{10}$$

these requirements on shear translate readily to requirements on ellipticity. However for this study we are interested in exploiting our relatively unbiased measurements of the position angles α. We therefore need to understand how biases in position angle measurements propagate into biases in the derived shear.

Survey	$\lvert m\rvert <$	$\lvert c\rvert <$
Stage II	0.02	0.001
Stage III	0.004	0.0006
Stage IV	0.001	0.0003

Table 5: Requirements on the systematic bias on shear components (γ_1 and γ_2), expressed in terms of the multiplicative (m) and additive (c) components of a linear bias model. Requirements are given for completed surveys ("Stage II" such as CFHTLens), intermediate-sized ongoing or future surveys ("Stage III" such as DES and SKA1) and for high-precision future surveys ("Stage IV" such as *Euclid* and SKA2).

Position angle-only shear estimators have recently been highlighted in Whittaker et al. (2014) and shown to be competitive with other current weak lensing estimators using the GREAT3 simulations in Whittaker et al. (2015a). We follow this work and apply the third order α-only shear estimator of Whittaker et al. (2014) to multiple realisations of a sample of galaxies. This shear estimator is given by (Whittaker et al. 2014)

$$\hat{\gamma} = \sqrt{\frac{32\sigma_e^2}{2\hat{F}_1^2 N^2}} \times \cos\left[\frac{1}{3}\left(\tan^{-1}\left(\sqrt{\frac{4\pi}{27e^{4\sigma_\alpha^2}\hat{F}_1^2} - 1}\right) + \pi\right)\right] \sum_{i=1}^{N} \boldsymbol{n(i)}, \tag{11}$$

where the vector $\boldsymbol{n(i)}$ is a 2-element vector composed of the sine and cosine of 2α for the i^{th} galaxy, σ_e is the intrinsic dispersion in galaxy ellipticities and N is the total number of galaxies in the sample. $F_1(|\hat{\gamma}|)$ is a function given by,

$$F_1(|\hat{\gamma}|) = e^{2\sigma_\alpha^2}\sqrt{\left[\frac{1}{N}\sum_{i=1}^{N}\cos(2\alpha^{(i)})\right]^2 + \left[\frac{1}{N}\sum_{i=1}^{N}\sin(2\alpha^{(i)})\right]^2}, \tag{12}$$

where σ_α is simply the intrinsic dispersion of measurement errors on the observed (sheared) position angles. The third order approximation (which requires inversion and interpolation of the $F_1(|\hat{\gamma}|)$ function) is a good approximation to the full estimator of Whittaker et al. (2014) in the regime $|\boldsymbol{\gamma}| \lesssim 0.2$.

In order to relate the accuracy with which we can recover position angles (as demonstrated in Figure 5) to the requirements on shear recovery for representative weak lensing experiments (as listed in Table 5), we have applied the third-order position-angle only shear estimator to a set of simple simulations that include linear shear biases in the simulated position angles.

We simulate position angle measurements with varying levels of intrinsic linear bias in α, in the range of $-0.2 < m_\alpha < 0.2$ and $-0.2 < c_\alpha < 0.2$. This was sampled using a gridded mesh of 200×800 upon the m_α and c_α parameter space to select input values, totalling $160,000$ realisations. For each realisation value we simulate a shear catalogue of $10,000$ galaxy shapes, each with a known gravitational shear component added to the galaxy shapes (where $e_i^{\rm sky} = e_i^{\rm int} + \gamma_i$). We then calculate the true position angles of the simulated galaxies ($\alpha_i^{\rm sky}$) using Equation (7) and add a position-angle measurement bias according to:

$$\alpha_i^{\rm obs} = (m_\alpha + 1)\alpha_i^{\rm sky} + c_\alpha, \tag{13}$$

where $\alpha_i^{\rm obs}$ is now the "observed" galaxy position angle (including both shear and bias effects). We then apply the third order position-angle only shear estimator described above to estimate the shear from our simulated position angle measurements. We repeat this process for several input shear values in order to fit a linear bias model for the estimated shear. The resultant shear bias parameters can then be compared to the shear bias requirements of Table 5 in order to place corresponding requirements on the bias in position angle measurements, i.e. on m_α and c_α. Figure 6 in Section 4.1.2 shows the bias in the estimated shear that results from the position angle bias for a range of position angle bias parameters. The performance of the position-angle recovery from the VLA-COSMOS simulations (see Section 4.1) and the requirements of Table 5 are also indicated on this figure.